



Azimuthal orientation guided topological defect evolution across the nematic-smectic phase transition

Jin-Bing Wu, Sai-Bo Wu, and Wei Hu ^{*}

National Laboratory of Solid State Microstructures, Key Laboratory of Intelligent Optical Sensing and Manipulation, College of Engineering and Applied Sciences, Nanjing University, Nanjing 210023, China

 (Received 30 June 2023; accepted 22 November 2023; published 11 December 2023)

Topological defects are of fundamental interest to wide branches of physics. Exploiting the structural evolutions and behaviors of topological defects across the phase transition is vital in understanding complicated condensed matter. Via presetting different initial azimuthal orientations of a square radial-alignment lattice in a hybrid cell, the evolution of liquid-crystal topological defects across the nematic-smectic phase transition is investigated. Distinct species of disclination lines are achieved in nematic phase via varying the initial azimuthal orientations. After cooling, various deformed toric focal conic domain arrays are generated as a result of the unique symmetry restriction and the suppression of twisted deformation in smectic phase. Different metastable crossed walls are formed due to the inheritance of orientational order when reheating to nematic phase. Transformations among these textures are observed under a microscope. The Landau–de Gennes theory is adopted to analyze the corresponding director distributions and defect evolutions. The underlying mechanism and laws of defect-species variation along with the change in azimuthal orientation are clarified and summarized. This study enriches the knowledge on self-organized ordered systems and may inspire intriguing applications.

DOI: [10.1103/PhysRevB.108.224107](https://doi.org/10.1103/PhysRevB.108.224107)

I. INTRODUCTION

Topological defects are determined just by the order symmetry and regardless of the scale of the system [1]. They are universal in wide branches of physics, including condensed matter [2], active matter [3], quantum systems [4], photonics [5], and even cosmology [6]. For condensed matter, topological defects are unavoidable consequences in continuous symmetry-breaking phase transitions [7]. Behaviors of topological defects and their transformations during phase transitions have attracted intensive attention from scientists [8,9]. Liquid crystals (LCs) are regarded as ideal model systems for corresponding research due to two facts: First, they are rich in topological defects and phases [10]; second, the evolution of topological defects commonly occurs in milliseconds to seconds and can be directly observed under a polarized optical microscope (POM), drastically facilitating the studies compared to micro- or cosmological analogs.

The nematic phase (N) of LC can be considered as an orientationally ordered fluid. In equilibrium, point and line disclinations emerge due to the orientational discontinuity of director n , which depicts the local average molecular orientation. Wall defects are another typical defect species existing at the boundary between domains of opposite orientations. Topological charge is usually $\pm 1/2$ or ± 1 in the former two cases, while it equals to 0 in the latter case [11]. In addition, spatial dimensions play important role in physics of topological defects. For example, $+1/2$ and $-1/2$ disclinations in LCs are topologically distinct as two dimensional (2D)

but topologically equivalent as three dimensional (3D), and the corresponding 3D topological charge is integer number [12]. Topological defects have great potential in microlens arrays [13], vortex beam generators [14], and particle manipulations [15]. Strategies such as properly presetting the surface alignments [16], alignment singularities on both substrate and superstrate [17], and azimuthally designing alignment patterns [18] on opposite substrates have been developed to improve the generation and manipulation of topological defects. Meanwhile, unidirectional easy orientation rewriting on one substrate [19] and external fields [20] has been adopted to direct the transformation of topological defects. Across the temperature-driven N-smectic (S) phase transition, a continuous symmetry breaking occurs, a one-dimensional positional order is additionally introduced, and the LC molecules arrange parallel to each other to form nanometer-thick layers. Under antagonistic boundary conditions (i.e., hybrid alignment conditions), these layers are periodically wrapped to generate toric focal conic domains (TFCDs) [21,22]. Such hierarchical configurations are promising in superhydrophobic surfaces [23], nanoparticle matrices [24], and microlens arrays [25,26]. Very recently, ordered TFCDs were converted from nematic LCs (NLCs) with disclination line arrays after several thermal cycles across the N-S phase transition. When reheated to the N phase, TFCDs change to a metastable state featured by crossed walls due to the inheritance of orientational order [27]. Till now, the mechanisms and laws of the evolution of topological defects across the phase transition have kept being a frontier of study and further investigation is beneficial for potential applications.

In this work, we investigate the topological defect evolution of LCs across the N-S phase transition in a hybrid cell

^{*}huwei@nju.edu.cn

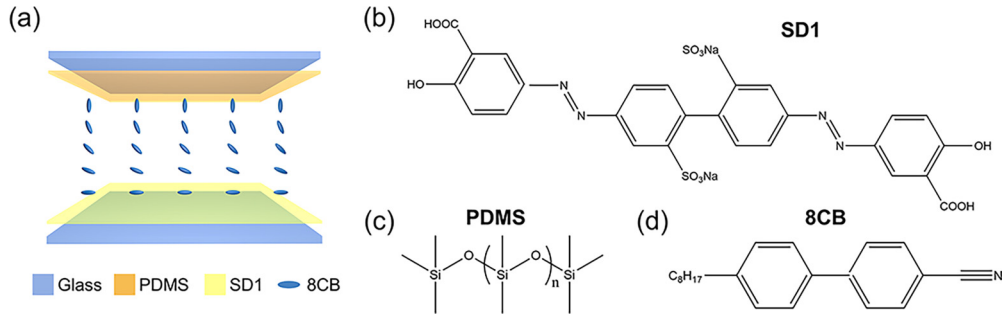


FIG. 1. (a) Schematic illustration of the hybrid cell. Molecular structures of (b) SD1, (c) PDMS, and (d) 8CB.

via varying the preset azimuthal orientation in square radial-alignment lattices in a hybrid cell via presetting azimuthal orientations. A square lattice of radial alignments is imprinted by photoalignment on the substrate, and a vertical alignment is set on the superstrate. For such an LC cell, disclination lines are formed during rapid cooling to the N phase from an isotropic state. Via varying the azimuthal orientation of the alignment unit, the type of disclination lines changes from twisted type to wedge type through a series of mixed types accordingly. The ordered TFCDs attained after several thermal cycles across the N-S phase transition convert to wall defects due to the inheritance of orientational order. The evolution of TFCDs and wall defects according to the azimuthal orientation is also studied. The Landau-de Gennes numerical modeling is utilized to reproduce the director distributions of the different N states, which reveals the mechanism and laws for topological defect transformation. This work makes the topological defect evolution across the phase transition predictable and enriches the fundamental understanding of self-organized soft matter.

II. RESULTS AND DISCUSSION

A hybrid cell with cell gap $h = 8.8\mu\text{m}$ is used to provide an antagonistic boundary condition [Fig. 1(a)]. A thin polydimethylsiloxane (PDMS) layer is coated on the superstrate to perform vertical alignment, while the substrate covered by the photoalignment agent SD1 [28] gives planar anchoring. They work together to generate a hybrid alignment for infiltrated LC 8CB [molecular structures of SD1, PDMS, and LC 8CB are revealed in Figs. 1(b), 1(c), and 1(d), respectively].

A square lattice of alignment singularities is recorded in the SD1 layer using a multistep partly overlapping photoalignment technique [29]. The alignment distribution at the center of each unit is expressed as

$$\alpha(x, y) = \sum_i s_i \arctan \frac{y}{x} + \alpha_0 \quad (1)$$

where topological charge $s_i = +1$ (red dot in Fig. 2), and α_0 is a constant initial azimuthal orientation. Thus, a -1 singularity (blue dot in Fig. 2) is automatically formed where four radial alignments meet. Here, we set the lattice constant $l = 30\mu\text{m}$. After 8CB is injected in the isotropic phase, the cell is cooled down to the N phase at a rate of $-1^\circ\text{C}/\text{min}$. In this process, the azimuthal orientation of the LC near the SD1 layer follows the guidance of local alignment and gradually turns to a uniform vertical alignment on the

superstrate. The phase-transition temperature is as follows: isotropic -40.5°C –N -33.5°C –SmA -21.5°C –crystal.

We systematically vary α_0 of the alignment, and the generated N textures are observed under POM. When $\alpha_0 = 0^\circ$, the resulting texture exhibits a square lattice of azimuthally changed interference colors, and the center of each unit is precisely addressed by the preset alignment. To show the director field more vividly, a first-order retardation plate ($\lambda = 530\text{ nm}$) is inserted between the sample and the analyzers. As shown in the inset of POM image of Fig. 2(a) (also corresponding to the alignment area of the top row), magenta is observed where n is parallel or perpendicular to the polarizer, and cyan and yellow are observed where n is perpendicular and parallel to the fast axis of the λ plate, respectively [30]. The λ plate enhances the influence of the azimuthal angle and suppresses that of the tilt angle, thus is beneficial to investigate the azimuthal variation of n . The magenta, cyan, and magenta emerge counterclockwise around the central $+1$ alignment singularity in each unit, indicating n distributions strictly follow the guidance of anchoring conditions. Notably, diagonal disclination lines are observed across the whole alignment region (yellow area in the inset). In this case, the integer defects decompose into pairs of half-integer defects to reduce the system energy, and disclination lines connect adjacent $+1/2$ and $-1/2$ defects accordingly (marked in orange dashed boxes). Then, we change α_0 to 30° , 60° , and 90° , respectively. As shown in Figs. 2(b)–2(d), the square lattice is always maintained, while the interference colors vary along with the change in α_0 . The insets show that the magenta-filled area gradually increases, indicating that n tends to arrange parallel or perpendicular to the polarizer, which is consistent with the presetting azimuthally alignment. These phenomena suggest that n twists with the change in α_0 . In addition, the disclination lines rotate counterclockwise slightly.

To get more insight in the director distribution and better understand the peculiar defect-transformation behaviors, we theoretically investigate the characteristics of the disclination line according to the Landau-de Gennes theory [31]. The nematic configuration is described by a traceless and symmetric tensor, defined as $Q_{ij} = S(n_i n_j - \frac{1}{3}\delta_{ij})$, where S represents the uniaxial scalar order parameter. The free-energy F of nematic LC is given by

$$\begin{aligned} F &= \int_v f dv + \int_s f_{\text{surface}} ds \\ &= \int_v (f_{\text{bulk}} + f_{\text{elastic}}) dv + \int_s f_{\text{surface}} ds. \end{aligned} \quad (2)$$

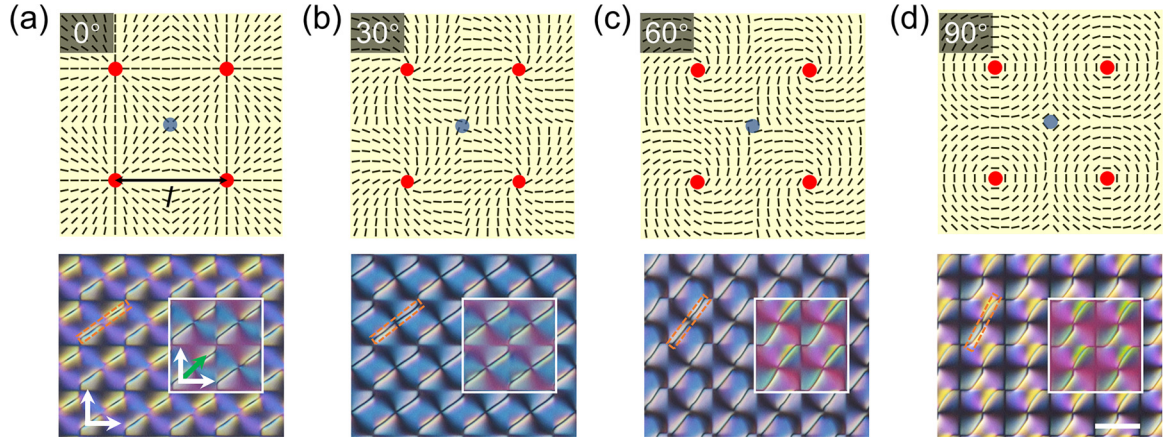


FIG. 2. Square lattice of alignment singularities with (a) $\alpha_0 = 0^\circ$, (b) $\alpha_0 = 30^\circ$, (c) $\alpha_0 = 60^\circ$, (d) $\alpha_0 = 90^\circ$ (top row), and corresponding POM images of the N phase at 34.0°C (bottom row). Insets show images observed with a λ plate. The white arrows denote the directions of a pair of crossed polarizers. The green arrow denotes the direction of the λ plate. The position of disclination lines is marked in orange dashed boxes. The scale bar indicates $30\ \mu\text{m}$ for all images.

The bulk energy f_{bulk} associated with the degree of nematic order, is written as:

$$f_{\text{bulk}} = \frac{1}{2}A\text{tr}Q^2 - \frac{1}{3}B\text{tr}Q^3 + \frac{1}{4}C(\text{tr}Q^2)^2. \quad (3)$$

In f_{bulk} , $A = A_0(T - T^*)$, where T^* is the nematic supercooling temperature, and A_0 , B , and C are constants. From Eq. (3), we can calculate the uniaxial scalar order parameter for the bulk equilibrium state,

$$S_{\text{eq}} = \frac{B}{4C} \left(1 + \sqrt{1 - \frac{24AC}{B^2}} \right),$$

which also depends on the temperature.

The f_{elastic} is the anisotropic elastic contribution to the free energy and accounts for any spatial gradients of Q . It is expressed by

$$f_{\text{elastic}} = \frac{1}{2}L_1 \frac{\partial Q_{ij}}{\partial x_k} \frac{\partial Q_{ij}}{\partial x_k} + \frac{1}{2}L_2 \frac{\partial Q_{ij}}{\partial x_j} \frac{\partial Q_{ik}}{\partial x_k} + \frac{1}{2}L_4 Q_{ij} \frac{\partial Q_{kl}}{\partial x_i} \frac{\partial Q_{kl}}{\partial x_j} + \frac{1}{2}L_{24} \left(\frac{\partial Q_{jk}}{\partial x_i} \frac{\partial Q_{ik}}{\partial x_j} - \frac{\partial Q_{ij}}{\partial x_j} \frac{\partial Q_{ik}}{\partial x_k} \right), \quad (4)$$

where the coefficients L_i ($i = 1, 2, 4, 24$) are related to the splay (k_{11}), twist (k_{22}), bend (k_{33}), and saddle-splay (k_{24}) elastic constants in Frank theory, and the relationships between them are

$$L_1 = \frac{3k_{22} - k_{11} + k_{33}}{6S_{\text{eq}}^2}, \quad L_2 = \frac{k_{11} - k_{22}}{S_{\text{eq}}^2},$$

$$L_4 = \frac{k_{33} - k_{11}}{2S_{\text{eq}}^2}, \quad L_{24} = \frac{k_{24}}{S_{\text{eq}}^2}. \quad (5)$$

The second integral in Eq. (2) contains the homeotropic anchoring contribution from the superstrate (PDMS) and the planar anchoring attribute to the bottom (SD1) interface. Homeotropic anchoring is modeled through a Rapini-Papoular expression: $f_{\text{surface}} = \frac{1}{2}W_h \text{tr}(Q - Q_s)^2$, where W_h is the anchoring energy and Q_s is the tensor preferred by the surface. Planar anchoring is modeled based on the form $f_{\text{surface}} = \frac{1}{2}W_p(\tilde{Q}_{ij} - \tilde{Q}_{ij}^\perp)(\tilde{Q}_{ij} - \tilde{Q}_{ij}^\perp)$, where $\tilde{Q}_{ij} = Q_{ij} + \frac{1}{2}S_{\text{eq}}\delta_{ij}$, using the projection operator: $\tilde{Q}_{ij}^\perp = P_{ik}\tilde{Q}_{kl}P_{lj}$, $P_{ij} = \delta_{ij} - v_i v_j$.

The tensor P_{ij} subtracts out the normal of the Q tensor and v is the substrate normal.

The free energy F is minimized according to the Euler-Lagrange equation solved by a finite-difference method. The parameters are chosen as $A = -0.172 \times 10^6\ \text{J/m}^3$, $B = 2.12 \times 10^6\ \text{J/m}^3$, and $C = 1.73 \times 10^6\ \text{J/m}^3$, leading to a scalar order parameter $S_{\text{eq}} = 0.533$. The homeotropic anchoring strength for the PDMS superstrate and the planar anchoring strength for the SD1 substrate are $W_h = 6 \times 10^{-6}\ \text{J/m}^2$ and $W_p = 1 \times 10^{-4}\ \text{J/m}^2$ [32], respectively. We choose $k_{11} = k_{33} = 2k_{22} = 9.5 \times 10^{-12}\ \text{N}$ and $k_{24} = k_{22}$ in our simulation. The simulation is performed on a cubic lattice with periodic boundary conditions in two lateral directions.

Figure 3(a) gives the 3D director field of the N texture obtained with the alignment shown in Fig. 2(a) and schematically sketches the key geometrical and topological features presented by the numerical simulation. To study the peculiar defect transformation, we present n distributions of two typical cross sections [as black and blue frames marked in Fig. 3(a)]. The black one is an x - y cross section of the middle layer, and the blue one is a cross section cutting the middle and additionally normal parallel to the tangent of the disclination line. Here, we define φ as the azimuthal component of the angle between n and the blue cross section. Figure 3(b) reveals director fields and φ distributions of marked cross sections. Simulations reveal that the n distribution in black cross section is consistent with the interference color variations in the POM images, and each disclination line connects adjacent $+1/2$ and $-1/2$ defects [33,34]. The discontinuous n and φ distributions in the blue cross section indicate that disclination lines are bent lines from the lower substrate towards the middle of the cell [as yellow circle marked in Figs. 3(b)–3(e)]. The n and φ distributions of LC textures with $\alpha_0 = 30^\circ$, 60° , and 90° are presented in Figs. 3(c)–3(e). The results in black cross sections show that φ changes with the variation of α_0 , consistent with the interference color variations in POM images (Fig. 2). The results in blue cross sections reveal that n is vertical above the middle of all disclination lines. Additionally, the n and φ distributions are distinct for samples with different α_0 , suggesting that the type of disclination line changes.

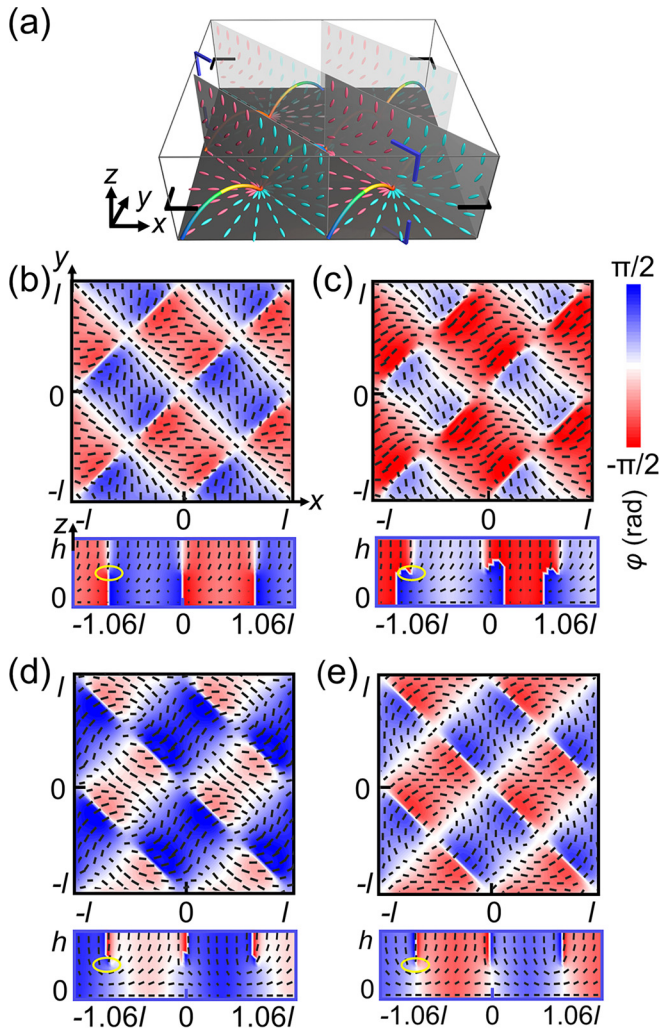


FIG. 3. (a) Three-dimensional illustration of disclination lines and director distribution in the N phase when $\alpha_0 = 0^\circ$. Simulated director fields and calculated φ distributions of the marked sections when (b) $\alpha_0 = 0^\circ$, (c) $\alpha_0 = 30^\circ$, (d) $\alpha_0 = 60^\circ$, and (e) $\alpha_0 = 90^\circ$. Yellow circles mark the locations of disclination lines.

To further investigate the transformation of the type of disclination lines, we analyze n distributions in three typical cross sections, as shown in Fig. 4(a). The t is defined as the tangent unit vector along the disclination line, and conventionally points toward the $-1/2$ defect. The Ω depicts a unit vector of the rotation axis of n winding around the disclination line, and it varies along the disclination line. The angle between t and Ω is defined as β [19]. According to the value of β , disclination lines can be classified into three different species; wedge type and twist type are corresponding to $\beta = 0, 180^\circ$, and $\beta = 90^\circ$, respectively, while other β values are attributed to mixed ones. Figures 4(b)–4(e) present the n distributions in three typical cross sections with $\alpha_0 = 0^\circ, 30^\circ, 60^\circ$, and 90° , respectively. Red and blue frames exhibit the n distributions of $+1/2$ and $-1/2$ defects, separately. They maintain wedge types, while n rotates counterclockwise and clockwise with an angle of $2\alpha_0$. Along with varying of $\pm 1/2$ defects on the substrate, the n distributions in green frames change as well. When α_0 changes from 0° to 90° , $\beta = 90^\circ - \alpha_0$. Therefore,

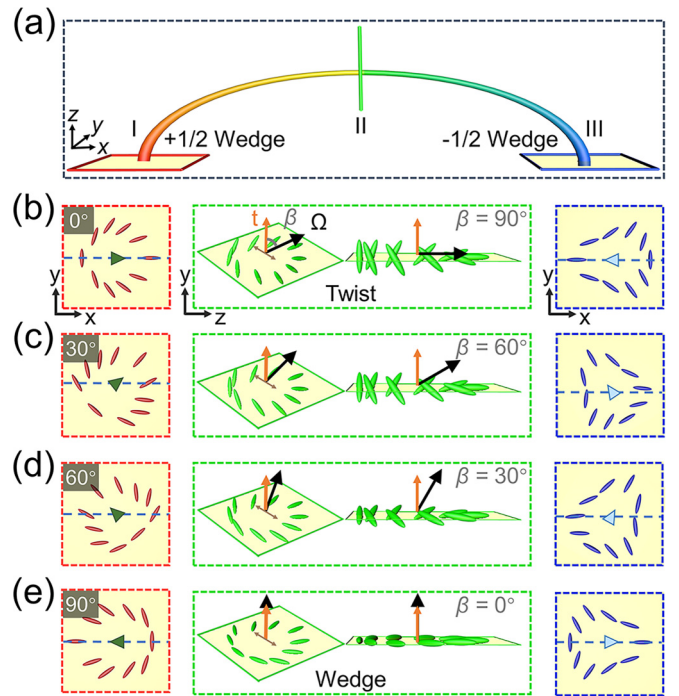


FIG. 4. (a) Three-dimensional illustration of one disclination line and three typical cross sections: I. $+1/2$ wedge profile, II. the middle profile, and III. $-1/2$ wedge profile. Transformations of disclination-line types in three typical cross sections when (b) $\alpha_0 = 0^\circ$, (c) $\alpha_0 = 30^\circ$, (d) $\alpha_0 = 60^\circ$, and (e) $\alpha_0 = 90^\circ$.

the disclination line varies from twist type to wedge type gradually through a series of mixed types. By combining the experiments and simulations, we find that a continuous transformation of disclination-line types (i.e., twisted type to wedge type through a series of mixed types) can be achieved by varying the initial azimuthal orientations.

As verified in our previous work [27], the above N phases with disclination lines will transform to ordered TFCDs with a lattice constant of l after several thermal cycles across the N-S phase transition when $\alpha_0 = 0^\circ$ [Fig. 5(a)]. For each TFCD, it consists of a family of smectic layers shaped as nested tori, with a circular defect line at the center of the tori and a vertical cusp line in the center of each unit [as shown in the upper right inset of Fig. 5(a)]. The radial alignment matches the infinite rotational symmetry of the TFCD unit and the hybrid alignment of LCs corresponds to the layer curvature variation, and thus facilitates the emergence of TFCD. After reheating to the N phase, crossed walls with a lattice constant of l are transformed with centers located at $+1$ singularities (the wall defects appear in the form of repeated crossed shape). The metastable texture emerges due to the inheritance of the orientational order from the TFCD texture. Figure 5(b) reveals that TFCDs are almost decomposed into four partial lobes, which rotate counterclockwise by $2\alpha_0$ when $\alpha_0 = 30^\circ$. We call this texture spiral TFCD. The lower right insets vividly illustrate the evolution of four partial lobes in each TFCD unit. When transformed to crossed walls, both the horizontal and vertical walls are twisted as well. Upon further increasing α_0 to 60° , disordered FCDs emerge instead of spiral TFCDs after thermal cycles. Fortunately, such frustrated FCDs will trans-

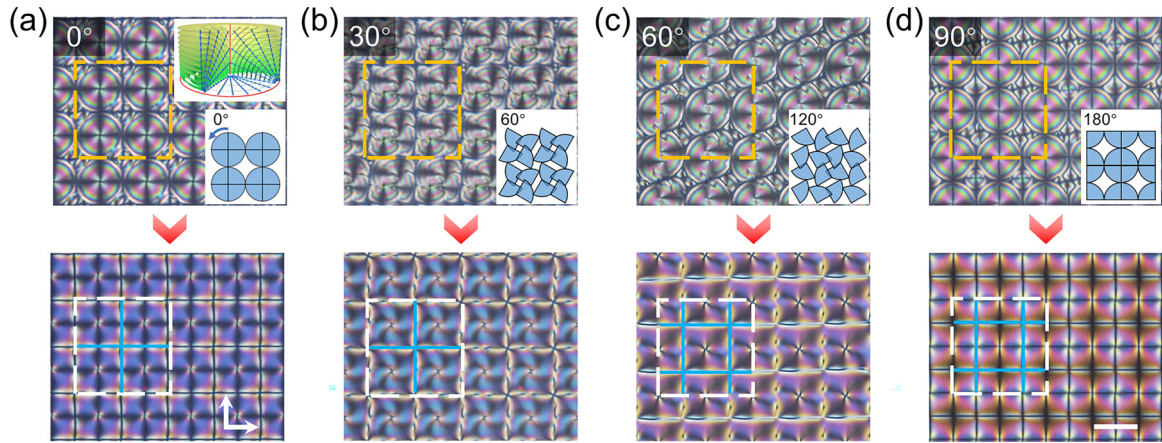


FIG. 5. TFCDs and split TFCDs in the S phase observed at 33.2°C (top row) and corresponding crossed walls in the N phase at 34°C (bottom row) when (a) $\alpha_0 = 0^\circ$, (b) $\alpha_0 = 30^\circ$, (c) $\alpha_0 = 60^\circ$, and (d) $\alpha_0 = 90^\circ$. The upper right inset in (a) exhibits the layered configuration and director distribution corresponding to a single TFCD. The lower right insets illustrate the evolution of TFCD units. The white arrows denote the directions of a pair of crossed polarizers. The scale bar indicates $30 \mu\text{m}$ for all images.

form to rotated partial TFCD lobes under mechanical pressing at 0.5°C below the N-S phase-transition point [Fig. 5(c)]. Moreover, four lobes adjacent to a -1 singularity arrange together to form a spiral TFCD. Namely, the obtained TFCDs shift for $l/2$ in both the horizontal and vertical directions. Here, the mechanical action accelerates the elimination of dislocations with high elastic energy and minimization of

the system energy. After reheating to the N phase, crossed walls emerge. Notably, the horizontal and vertical walls are different due to the symmetrical differences of the shifted spiral TFCDs, and the positions of the walls shift $l/2$ accordingly. Figure 5(d) shows the case of $\alpha_0 = 90^\circ$. TFCDs with infinite-axis rotation symmetry emerge again, and shift $l/2$ in both the horizontal and vertical directions. The crossed

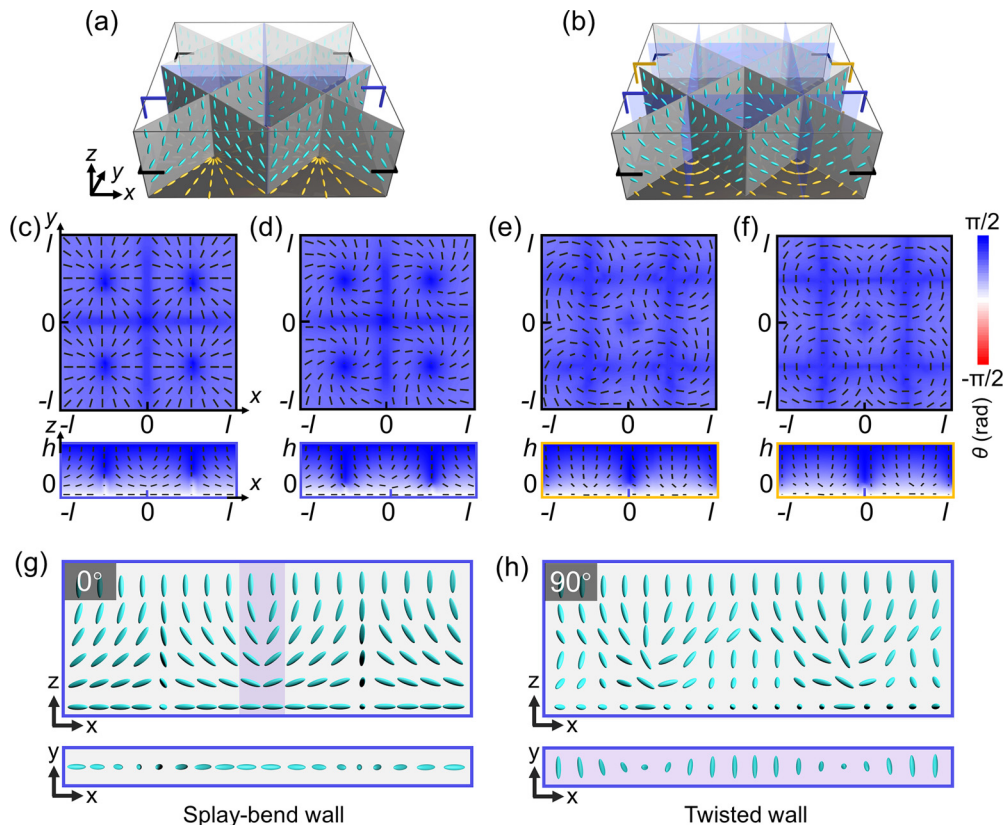


FIG. 6. Three-dimensional illustrations of (a) crossed wall when $\alpha_0 = 0^\circ$ and (b) laterally shifted crossed wall when $\alpha_0 = 90^\circ$. Calculated n and θ distributions of marked sections when (c) $\alpha_0 = 0^\circ$, (d) $\alpha_0 = 30^\circ$, (e) $\alpha_0 = 60^\circ$, and (f) $\alpha_0 = 90^\circ$. Three-dimensional illustrations of (g) the splay-bend wall and (h) twisted walls when $\alpha_0 = 0^\circ$ and 90° , respectively.

walls shift accordingly, and the interference colors are significantly different from those shown in Fig. 5(a). Our experiment results show that $\alpha_0 = 45^\circ$ is the transition point for the $l/2$ shift.

We further simulate n distributions of the N phase with crossed walls along with α_0 variation. Figures 6(a) and 6(b) give 3D n distributions when $\alpha_0 = 0^\circ$ and $\alpha_0 = 90^\circ$, respectively. We define θ as the polar angle between the n and z axis. Figures 6(c)–6(f) reveal the simulated n and θ distributions in the marked sections of Figs. 5(a)–5(d), respectively. According to the simulations, n twists with α_0 changing in x - y cross sections and leads to the deformation of crossed walls. The $l/2$ position shifts of the crossed walls in both the horizontal and vertical directions are consistent with experiments at $\alpha_0 = 60^\circ$ and 90° , respectively. Further considering θ distributions in x - z cross sections, we find that crossed walls change from splay-bend type to twisted type [Figs. 6(g) and 6(h)], corresponding to the blue-frame marked sections in Figs. 6(a) and 6(b)]. We use n distributions in the x - z and x - y cross sections to analyze the type of walls. The splay-bend wall involves only the splay and bend deformations, while twist deformation also exists in twisted walls.

III. CONCLUSION

The topological-defect evolution of the LC across the N-S phase transition is investigated via presetting the initial azimuthal orientation of a square radial-alignment lattice in a hybrid cell. The Landau–de Gennes theory is adopted to analyze the director distributions and defect transformations. Along with α_0 increasing from 0° to 90° , the

gradually enhanced twisted deformations of n in N phase make disclination lines changing from twisted type to wedge type through a series of mixed types with a rigid dependency on α_0 . However, twisted deformation is suppressed in S phase. After cooling to the S phase, discontinuous LC layers are formed due to the inheritance of orientation order, resulting in various deformed TFCDs. Spiral TFCDs with four partial lobes are obtained when $\alpha_0 < 45^\circ$. For cases of $\alpha_0 > 45^\circ$, spiral TFCDs shift $l/2$ in both the horizontal and vertical directions. When $\alpha_0 = 90^\circ$, TFCDs with infinite-axis rotation symmetry emerge again with an $l/2$ lattice shift. When the above TFCDs reheat to the N phase, splay-bend type crossed walls are formed when $\alpha_0 < 45^\circ$, while twisted crossed walls emerge for cases of $\alpha_0 > 45^\circ$. The defect transformation across the N-S phase transition is governed by the inheritance of orientation order. This work discloses the mechanism and finds the laws behind the evolution of topological defects across the phase transition, making the evolution predictable and controllable. Our findings enrich the fundamental understanding of self-organized soft matter and may pave the way for advanced applications of topological defects.

ACKNOWLEDGMENTS

The authors gratefully acknowledge the support of the National Key Research and Development Program of China (Grant No. 2022YFA1203703), the National Natural Science Foundation of China (NSFC) (No. 62035008) and Fundamental Research Funds for the Central Universities (No. 021314380189 and No. 021314380233).

-
- [1] W. H. Zurek, *Nature (London)* **317**, 505 (1985).
- [2] C. Sheng, Y. Wang, Y. J. Chang, H. M. Wang, Y. H. Lu, S. N. Zhu, X. M. Jin, and H. Liu, *Light Sci. Appl.* **11**, 243 (2022).
- [3] C. H. Peng, T. Turiv, Y. B. Guo, Q. H. Wei, and O. D. Lavrentovich, *Science* **354**, 882 (2016).
- [4] C.-K. Chiu, J. C. Y. Teo, A. P. Schnyder, and S. Ryu, *Rev. Mod. Phys.* **88**, 035005 (2016).
- [5] Z. G. Chen and M. Segev, *eLight* **1**, 2 (2021).
- [6] I. Chuang, R. Durrer, N. Turok, and B. Yurke, *Science* **251**, 1336 (1991).
- [7] N. Mermin, *Rev. Mod. Phys.* **51**, 591 (1979).
- [8] M. A. Bates and D. Frenkel, *J. Chem. Phys.* **112**, 10034 (2000).
- [9] S. C. Kapfer and W. Krauth, *Phys. Rev. Lett.* **114**, 035702 (2015).
- [10] P. G. de Gennes and J. Prost, *Physics of Liquid Crystals* (Oxford University Press, New York, 1993).
- [11] K. Mauice and O. D. Lavrentovich, *Soft Matter Physics: An Introduction* (Springer-Verlag, New York, 2003).
- [12] O. D. Lavrentovich, *Liq. Cryst.* **24**, 117 (1998).
- [13] Y. H. Lin, H. S. Chen, H. C. Lin, Y. S. Tsou, H. K. Hsu, and W. Y. Li, *Appl. Phys. Lett.* **96**, 113505 (2010).
- [14] R. You, Y. S. Choi, M. J. Shin, M. K. Seo, and D. K. Yoon, *Adv. Mater. Technol.* **4**, 1900454 (2019).
- [15] L. L. Ma, C. Liu, S. B. Wu, P. Chen, Q. M. Chen, J. X. Qian, S. J. Ge, Y. H. Wu, W. Hu, and Y. Q. Lu, *Sci. Adv.* **7**, eabh3505 (2021).
- [16] Y. B. Guo, M. Jiang, S. Afghah, C. H. Peng, R. L. B. Selinger, O. D. Lavrentovich, and Q. H. Wei, *Adv. Opt. Mater.* **9**, 2100181 (2021).
- [17] H. Yoshida, K. Asakura, J. Fukuda, and M. Ozaki, *Nat. Commun.* **6**, 7180 (2015).
- [18] M. F. Wang, Y. N. Li, and H. Yokoyama, *Nat. Commun.* **8**, 388 (2017).
- [19] J. H. Jiang, K. Ranabhat, X. Y. Wang, H. Richb, R. Zhang, and C. H. Peng, *Proc. Natl. Acad. Sci. USA* **119**, e2122226119 (2022).
- [20] T. Ouchi, K. Imamura, K. Sunami, H. Yoshida, and M. Ozaki, *Phys. Rev. Lett.* **123**, 097801 (2019).
- [21] J. M. Xia, S. MacLachlan, T. J. Atherton, and P. E. Farrell, *Phys. Rev. Lett.* **126**, 177801 (2021).
- [22] H. Aharoni, T. Machon, and R. D. Kamien, *Phys. Rev. Lett.* **118**, 257801 (2017).
- [23] Y. H. Kim, D. K. Yoon, H. S. Jeong, J. H. Kim, E. K. Yoon, and H. T. Jung, *Adv. Funct. Mater.* **19**, 3008 (2009).
- [24] D. K. Yoon, M. C. Choi, Y. H. Kim, M. W. Kim, O. D. Lavrentovich, and H. T. Jung, *Nat. Mater.* **6**, 866 (2007).
- [25] L. L. Ma, S. B. Wu, W. Hu, C. Liu, P. Chen, H. Qian, Y. D. Wang, L. F. Chi, and Y. Q. Lu, *ACS Nano* **13**, 13709 (2019).
- [26] J. B. Wu, S. B. Wu, H. M. Cao, Q. M. Chen, Y. Q. Lu, and W. Hu, *Adv. Opt. Mater.* **10**, 2201015 (2022).
- [27] S. B. Wu, J. B. Wu, H. M. Cao, Y. Q. Lu, and W. Hu, *Phys. Rev. Lett.* **130**, 078101 (2023).

- [28] M. Schadt, K. Schmitt, V. Kozinkov, and V. Chigrinov, *Jpn. J. Appl. Phys.* **31**, 2155(1992).
- [29] P. Chen, S. J. Ge, W. Duan, B. Y. Wei, G. X. Cui, W. Hu, and Y. Q. Lu, *ACS Photonics* **4**, 1333 (2017).
- [30] M. J. Gim, D. A. Beller, and D. K. Yoon, *Nat. Commun.* **8**, 15453 (2017).
- [31] M. Ravnik and S. Zumer, *Liq. Cryst.* **36**, 1201 (2009).
- [32] H. Akiyama, T. Kawara, H. Takada, H. Takatsu, V. Chigrinov, E. Prudnikova, V. Kozenkov, and H. Kwok, *Liq. Cryst.* **29**, 1321 (2002).
- [33] S. Harkai, B. S. Murray, C. Rosenblatt, and S. Kralj, *Phys. Rev. Res.* **2**, 013176 (2020).
- [34] S. Harkai, C. Rosenblatt, and S. Kralj, *Crystals* **13**, 904 (2023).